



Effects of horizontal ground motion incident angle on the seismic risk assessment of a high-speed railway continuous bridge

Biao Wei^{1,2} · Zhangliang Hu^{1,2} · Chengjun Zuo³ · Weihao Wang^{1,2} · Lizhong Jiang^{1,2}

Received: 8 July 2020 / Revised: 6 December 2020 / Accepted: 21 December 2020 / Published online: 19 January 2021
© Wrocław University of Science and Technology 2021

Abstract

This study investigates the effects of horizontal ground motion incident angle on a high-speed railway continuous bridge (HSRCB). To that end, incremental dynamic analyses (IDA), seismic vulnerability analyses and seismic risk assessments were conducted on a three-span HSRCB subjected to a set of ground motions under five incidence angles θ (0° – 90°). The analysis was developed only from the perspective of PGA and the results showed that the longitudinal waves ($\theta=0^\circ$) only caused seismic responses in the longitudinal direction, while the waves in other directions, especially in the transverse direction, caused a coupling response both in longitudinal and transverse directions for some components, such as the sliding layer and CA mortar layer. The longitudinal seismic damage of the sliding layer and CA mortar layer under the transverse waves should receive more attention in seismic design since the exceeding probabilities and seismic risk probabilities under various incident angles θ are as high as the calculated value for $\theta=0^\circ$, and with a variation within 5.95%. The maximum variation of the longitudinal response and probability for track parts was within 10.59% under various incident angles, with a significant difference in the transverse response and probabilities in response to different incident angles. In addition, the responses of bridge structure components were more sensitive to the incident angles in comparison with the track parts. Finally, results indicate that the risk probabilities are at a maximum when the ground motions fall within horizontal orientations of 67.5° – 90° at the bridge longitudinal axis.

Keywords High-speed railway continuous bridge (HSRCB) · Horizontal ground motion direction · Vulnerability analysis · Seismic risk assessment

1 Introduction

A large proportion of track structure installed on bridges is a remarkable feature of China's high-speed railway network. For a railway network composed of numerous bridges, it is increasingly important to ensure their safety under earthquake scenarios. Seismic vulnerability and risk analysis has been used to evaluate the seismic performance of bridges. However, the results obtained using these methods are not only affected by the configuration of bridges, but also depend on variables like ground motion intensity and direction. Although high-speed railway bridges are designed to be located far away from known faults, in fact, they inevitably pass through some sites with seismic activity, which causes ground motions on horizontal components to be transmitted to the bridge from any orientation. This generates deviations to seismic performance evaluations for such bridges other than considerations of ground motion along bridge axes. Accordingly, it is crucial to carry out research on the

✉ Chengjun Zuo
11930949@mail.sustech.edu.cn

Biao Wei
weibiao@csu.edu.cn

Zhangliang Hu
huzhangliang@csu.edu.cn

Weihao Wang
wangweihao21@csu.edu.cn

Lizhong Jiang
lzhjiang@csu.edu.cn

¹ School of Civil Engineering, Central South University, 68 South Shaoshan Road, Changsha 410075, China

² National Engineering Laboratory for High Speed Railway Construction, 68 South Shaoshan Road, Changsha 410004, China

³ Department of Mechanics and Aerospace Engineering, Southern University of Science and Technology, 1088 Xueyuan Avenue, Shenzhen 518055, China

impact of the horizontal ground motion incident angle on high-speed railway bridges and to identify the most disadvantageous attack angle of horizontal ground motion with respect to the longitudinal axis of the bridge.

Some influences of the horizontal ground motion incident angle on the structural responses and vulnerabilities of bridges have been discussed in previous studies. Mackie et al. [1] conducted seismic elastic–plastic analysis on five different continuous and simply-supported highway bridges, and concluded that the incident angle of horizontal earthquake waves had no significant influence on the damage probabilities of such bridges. Ramanathan [2] stated that the incidence angle could be negated when dealing with non-skewed bridges with symmetric geometry. Taskari and Sextos [3] carried out a nonlinear time history analysis on a (27 + 45 + 27) m highway overpass continuous girder with a slope of 7%, and under horizontal earthquake scenarios with different attack angles ranging from 0° to 180° at a step of 15°. The results showed that the top of piers and abutments are more sensitive to the horizontal earthquake incident angle than the bottom of piers and bearings. Moschonas and Kappos [4] analyzed a symmetrical three-span bridge with two piers monolithically connected to the deck and with steel bearings seated on the abutments, their study having pointed out that the vulnerability of a bridge was the lowest when the earthquake attack angle is 60° and the greatest when subjected to transverse waves. Similarly, when the horizontal motion propagated 30° to 60° with respect to the longitudinal axis of the bridge, the seismic demands of a five span RC beam bridge were at a maximum [5]. Magliulo et al. [6] and Ni et al. [7] validated that the irregularity and complexity of structural shapes tended to result in an increased sensitivity to dynamic responses and greater vulnerability to the specific directions of ground motions, due to the interactions between bending and torsion. Moreover, some scholars have comprehensively investigated the influence of seismic intake angle and soil-structure interaction (SSI) on dynamic responses for bridges. Soltanieh et al. [8] found that irregular bridges were more sensitive to the directionality of ground motion in comparison with regular bridges, and that this sensitivity was variable in two foundation models, i.e. considering soil-structure interaction and assuming a fixed base. As well, Noori et al. [9] found that direction effects were more pronounced when SSI effects were taken into consideration, and furthermore revealed that the damage to components was as high as 77% when ground motions were applied in directions other than the longitudinal and transverse axes of a bridge. Based on quantitative analysis, Torbol and Shinozuka [10] concluded that the direction of ground motions could change the median values of damage probabilities from 22 to 66%. Furthermore, Araújo et al. [11] identified that the peak response of 3-dimensional curved bridges became more sensitive to the

direction of seismic excitations as the degree of curvature increased. In recent years, there has been a trend towards investigating the influences of the attack angle of ground motion on skewed bridges. Bhatnagar and Banerjee [12] evaluated the effects of the ground motion incidence angle on the seismic performance of a skewed bridge. Results were presented in terms of vulnerability curves and showed that a bridge's seismic vulnerability was insensitive to the ground motion incident angle. Similarly, Wang et al. [13] showed that both the far-field and near-field ground motions attack angle have little effect on skewed bridges. The influence of the incidence angle was further reduced for a skewed bridge equipped with buckling restrained braces. Finally, simulated results verified that the effects of incidence angle were more pronounced in integral bridges than those in skewed bridges [14].

In summary, the sensitivity of structural seismic responses to the ground motion incident angle produces inconclusive results since the effects depend on structural irregularities, the soil-structure interaction and the level of structural damage, among other concerns. However, until now there has been no literature focusing on the bridges in high-speed railway networks. In terms of the performance-based seismic design of high-speed railway bridges, there are still some deficiencies:

(1) When the bridge site is surrounded by faults, the ground motion from earthquakes generate inputs that feed into high-speed railway bridges in different horizontal directions. However, only the longitudinal seismic response caused by ground motion propagating along the longitudinal axis of a bridge and the transverse seismic response caused by transmission along the transverse axis of a bridge are generally analyzed, which may ignore the potential coupling effect of high-speed railway bridges under other horizontal ground motions.

(2) Previous analysis of seismic vulnerability in railway bridges has focused on damage to the bridge structure itself and has rarely analyzed damage to the track structure [15]. In comparison with traditional highway bridges, high-speed railway bridges increase the constraint of the track structure on the bridge, which has a significant impact on the natural frequency and its seismic response [16], all of which is especially indicative of continuous ballastless China Railway Track Slab II (CRTSII) structures [17].

Accordingly, by selecting a three-span pre-stressed continuous beam bridge with the continuous track structure CRTS II [18–20] as an example, this paper investigates the significance of considering different ground motion incidence angles by applying vulnerability analyses and seismic risk assessments. Firstly, a spatial integration calculation model for the track-bridge structure is developed using the OpenSEES platform. A series of scaled horizontal ground motion scenarios is employed under different attack angles θ ranging from 0°

to 90° at a step of 22.5° based on a nonlinear time history analysis. Then, the vulnerability surfaces are developed and combined with seismic hazard analyses, thereby obtaining the risk probabilities of bridge components. Finally, the impact of the earthquake angles on the structural responses and damage probabilities of track components and bridge components are discussed, which provide some further guidance for developing the layout, construction and seismic reinforcement of high-speed railway bridges in China [21, 22].

2 Analysis methodology

2.1 Methodology for seismic vulnerability

Seismic vulnerability refers to the probability of various failure states for structures given a specific value of ground motion intensity (IM_j). In general, structural vulnerability is defined by conditional probability, as shown in Eq. (1) [23]:

$$P_{ij} = P[D \geq C_i | IM_j] \quad (1)$$

where, D is seismic demand, obtained by nonlinear time history analysis. C_i is the capacity of the specified damage state. D and IM are both generally assumed as lognormal distributions, and thus, the functional relationship between D and IM can be expressed in Eq. (2) as follows [24]:

$$S_d = aIM_j^b \text{ or } \ln S_d = \ln a + b \ln IM_j \quad (2)$$

a and b in Eq. (2) are the linear regression parameters, which are obtained by linear regression analysis on the scatter plot of logarithmic D and IM_j , i.e., in log–log coordinate.

In Eq. (1), the capacity C_i is also assumed as a lognormal distribution, which means that the conditional probability is transferred as follows [25]:

$$P_{ij} = P[D \geq C_i | IM_j] = \Phi \left(\frac{\ln(S_d/S_{ci})}{\sqrt{\beta_d^2 + \beta_{ci}^2}} \right) \quad (3)$$

In Eq. (3), Φ is the standard normal distribution cumulative density function, S_d is the median value of the structural earthquake demand, calculated by Eq. (2); S_{ci} is the median value of capacity, listed in Table 5, while β_d and β_{ci} are the standard deviations for the structural demand and capacity, respectively [26].

$$\beta_d = \sqrt{\frac{\sum_{i=1}^N (\ln d_i - \ln S_d)^2}{N - 2}} \quad (4)$$

$$\beta_{ci} = \sqrt{\ln(1 + COV^2)} \quad (5)$$

where, d_i is the dynamic response obtained by nonlinear dynamic time history analysis under the action of the i -th seismic wave; N is the total number of seismic waves; COV is the coefficient of variation of the seismic capacity of the component, referring to the research of Nielson [27], the value is 0.25 with respect to slight and moderate damage state, and the value is 0.5 with respect to severe and complete damage state.

2.2 Methodology for seismic hazard analysis

Seismic hazard analysis is used to obtain the exceeding probability of earthquakes with different intensities during a given period of time.

By referring to the work of Gao and Bao [28], the extreme value type III distribution is a much better fit to the actual situation reflecting the probability distribution of earthquake intensity in China, and its probability can be expressed as follows:

$$F_{III}(i) = 1 - P(I \geq i) = \exp \left[- \left(\frac{\omega - i}{\omega - \varepsilon} \right)^k \right] (i \leq \omega) \quad (6)$$

where, $P(I > i)$ represents the annual probability of exceedance; i is the seismic intensity; ω represents the upper limit of seismic intensity, with the value using being 12 [29]; ε represents the mode intensity, that is, the earthquake intensity with a probability of exceeding 63.2% in the base period of 50 years; and, k is the shape parameter. From this, the occurrence probability of earthquake risk is obtained as Eq. (7).

$$P(I = i|T) = P(I \geq i|T) - P(I \geq i + 1|T) \quad (7)$$

where, $P(I=i|T)$ represents the probability of occurring intensity i within a 100-year fortification standard; $P(I \geq i|T)$ represents the probability of exceeding intensity i within a 100-year fortification standard.

In this paper, the seismic basic intensity at the bridge site is taken as 8 degrees, which means that the value of the shape parameter k is 6.8713 [30]. The probability values of the average occurrence of each seismic intensity for the site during the 100-year reference period are also calculated and have been listed in Table 1.

Based on this, the seismic risk assessment can be written using the potential risk probability of failure states between the capacity limits C_i and C_{i+1} when considering the possibility of earthquakes occurring with different intensity levels at a certain bridge site, as follows [31]:

Table 1 Occurrence probability of each earthquake intensity level (at a seismic basic intensity of 8 degrees)

Terms	Values				
PGA/g	0.05	0.1	0.2	0.4	0.8
Ln(PGA)	-2.996	-2.303	-1.609	-0.916	-0.223
Probability/%	3.28	34.39	43.33	16.12	2.70

$$P_i = \sum_{j=1}^{j=n} (P[D \geq C_i | IM_j] - P[D \geq C_{i+1} | IM_j]) P[IM_j] \quad (8)$$

where, $P[IM_j]$ is the occurrence probability of a j -intensity earthquake.

Note: The representative values of peak ground acceleration in areas with the basic intensities of 6, 7, 8, 9 and 10 degrees are 0.05, 0.1, 0.2, 0.4 and 0.8 g, respectively.

The details of the calculation process for incremental dynamic analyses, vulnerability analyses and seismic risk analyses are shown below:

Step 1: Sect. 3.2 developed a numerical model for an example of a high-speed railway bridge.

Step 2: Sect. 3.3 selected 20 actual seismic records and scaled them to different IM, then discussed the engineering demand parameters (EDP) and determined their damage indicators.

Step 3: Sect. 4.1 conducted time history analysis and indicated the relationship between the EDP and the IM.

Step 4: Sect. 4.2 depicted the vulnerability curves of selecting EDPs both in longitudinal and transverse directions.

Step 5: Sect. 4.3 calculated the risk probabilities of a certain failure state when considering the occurrence possibility of earthquakes.

3 Analysis of HSRCB underground motions with different attack angles

3.1 General description of the bridge

A three-span pre-stressed continuous beam bridge with continuous track structure CRTS II is analyzed in this paper, with the configuration plotted in Fig. 1. The span of the bridge is 48 + 80 + 48 m, and three simply supported beams with a span of 32 m are arranged at both ends. The deck is a C50 concrete single box single chamber section, and its height changes by quadratic parabola. According to the code of bridge design by Chinese criterion [32], the section height of girder at the middle span is (1/1.5 ~ 1/2.5) of the section height at the bearings. The increase in the section height of the girder at the bearings not only can resist the shear force delivered by the bearings but also reduces the bending moment at the mid-span position, and the mid-span section mainly bears the bending moment, so the section height of girder at the bearings (Section II-II) is greater than that at the mid-span position (Section III-III). Moreover, the shear force and negative bending moment of the girder at the bearing position are relatively large, so the section web and bottom plate should be thickened. Therefore, the thickness of the web and bottom plate of the girder section at the bearings position (Section I-I and Section II-II) is greater than that of the mid-span section (Section III-III). The actual spherical

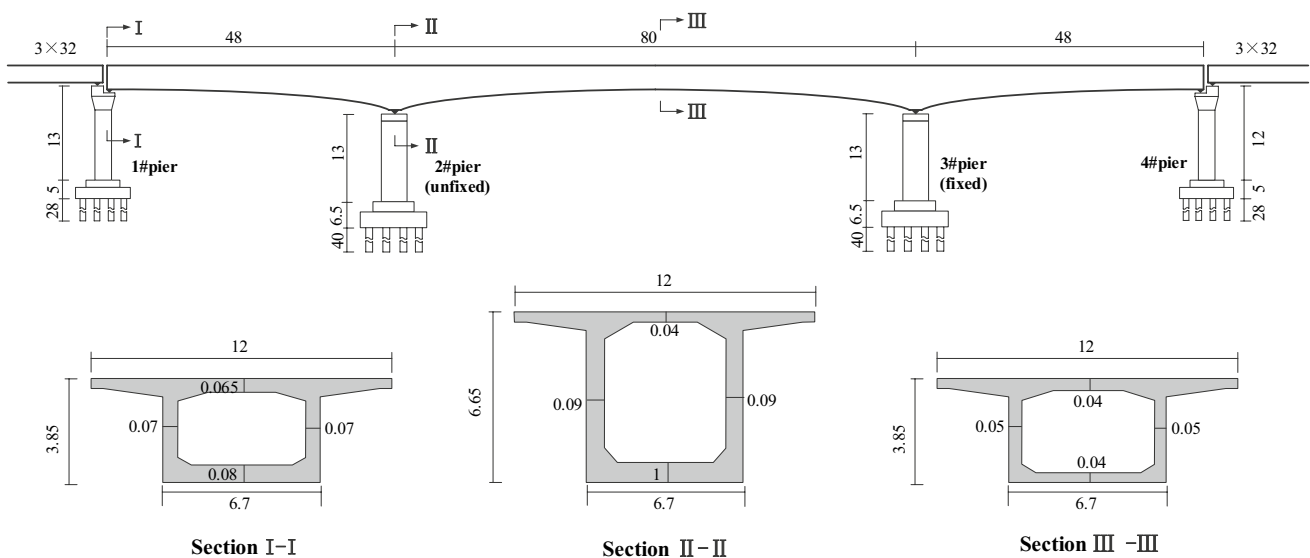


Fig. 1 Configuration of a three-span HSRCB (unit: m)

bearings arrangement is shown in Fig. 2. Only the longitudinally fixed bearings are arranged between the deck and No. 3 pier while other positions are set up with longitudinal sliding bearings. Moreover, pile group foundations with C30 concrete circular sections are arranged under each pier.

Figure 3 is the detailed layout of the ballastless track slab (CRTS II) recommended by Chinese criterion [18, 33]. Being the primary supporting members of the track structure, the base plate is therefore made of C30 concrete. Shear grooves and shear studs are used to ensure a reliable connection between the base plate and the girder (in Fig. 3). Furthermore, to limit and buffer the vertical and horizontal displacement of the base plate, lateral blocks are also set on the bridge deck. The sliding layer between the deck and the base plate is in the form of two layers of geotextile sandwiched with one layer of geomembrane. The thickness of the middle layer of geomembrane is 1 mm, and the thickness of the upper and lower layers of geotextile are 3 mm and 2 mm, respectively. The setting of shear grooves and slots ensures a reliable connection between the deck and the base plate, and limits the free sliding of the base plate on the sliding layer. On the top of the base plate is the track plate, which runs continuously along the longitudinal direction of the bridge. Each standard CRTS II track slab is 6.45 m in length, 2.55 m in width and 0.2 m in thickness, and is precast using concrete C55. A 0.3 m CA mortar layer is filled in between the track plate and the base plate, which acts as a kind of buffer material or structural layer with a certain defined elasticity, while shear reinforcement is set at the girder end to connect with the base plate. The steel rail is connected to the track plate through WJ-8C fasteners with a spacing of 0.65 m.

3.2 Bridge numerical model

Based on the OpenSEES platform [34], a three-dimensional integration analysis model is developed that take into consideration both the bridge structure and track structure. Generally, the vertical force of the superstructure caused by the earthquake is not significant, and the superstructure with strong vertical bearing capacity is mainly used to bear the vertical load, so the superstructure remains elastic in case of

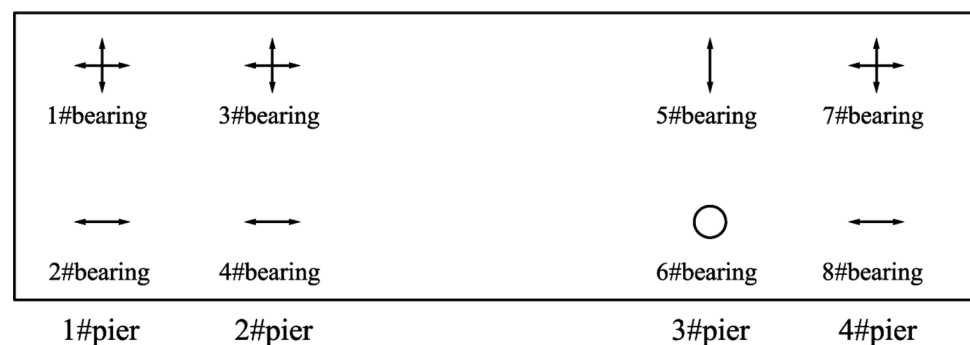
an earthquake. Thus, the elastic beam-column elements in OpenSEES [34] are applied to simulate rails, the track plate, the base plate and the girder.

Non-linear beam-column elements are applied to simulate the cross section of piers and piles, which is discretized into the protective layer of concrete, longitudinal steel bars and the confined concrete. The stress–strain relationship of the confined concrete and the protective layer of concrete is defined using the Mander model [35] [in Fig. 4b], and the stress–strain constitutive of longitudinal reinforcements adopts the Giuffrè-Menegotto’s isotropic strain hardening–Pinto model [36], as depicted in Fig. 4b. The key parameters of concrete and steel material are summarized in Table 2 and Table 3, respectively.

Non-linear beam-column elements are used to simulate each sub-pile structure in the group pile foundation, with three translational and three rotational soil springs applied at each node of the pile to consider the interaction between the pile and the soil. According to the “*m*” method [22], the six soil springs’ stiffness can be derived. Based on the Winkler assumption, the lateral soil resistance of a pile at a certain depth is proportional to the horizontal deflection at that depth. Thus, the spring stiffness can be readily calculated, though the calculation process for each spring stiffness value has been omitted here due to space limitations.

The connecting components in track structures, including the sliding layer, the CA mortar layer, rail fasteners, lateral blocks and bearings, can slide under the action of an earthquake. It is more critical to define the force displacement relationship accurately than to simulate its actual shape. In OpenSEES, Zerolength element defined by two nodes at the same location can be endowed with multiple UniaxialMaterial objects to represent the force–deformation relationship. Therefore, using Zerolength element can accurately simulate such connecting components without considering its complex actual shape. The force displacement relationship is depicted in Fig. 4a, and is set following the actual constitutive model of these components. According to the Chinese criteria [22], the horizontal yield force F_y and the yield displacement d_y of the spherical steel bearing in the fixed direction and sliding direction are calculated, listed

Fig. 2 Layout of bearings



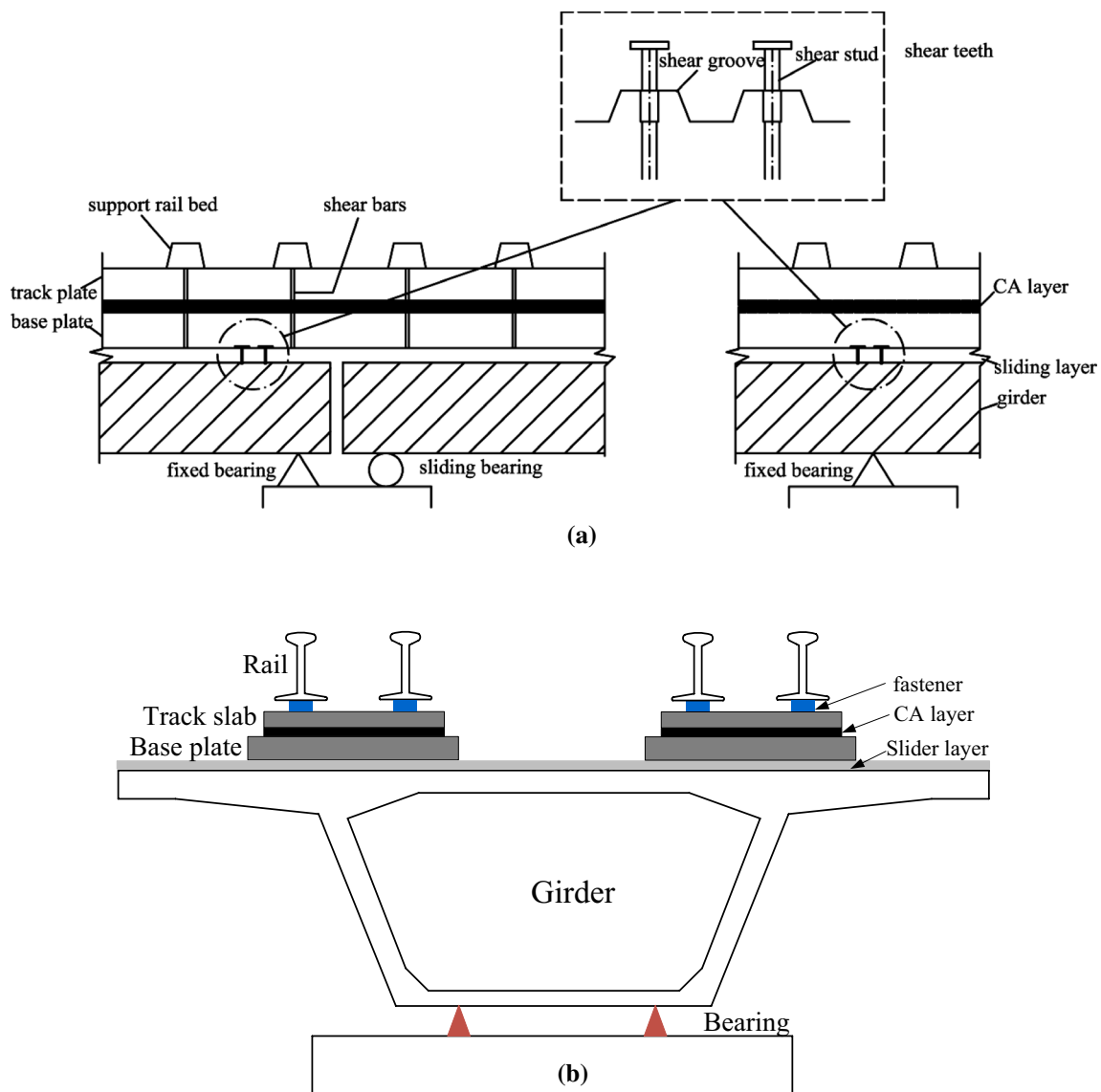


Fig. 3 Detailed overview of the CRTS II: (a) along the longitudinal direction of the bridge and (b) along the transverse direction of the bridge

in Table 4. Based on the test results of sliding layer in [33], the values of F_y and the d_y are 6.0 kN and 0.0005 m, respectively. Longitudinal resistance test of fasteners shows that the yield point displacement d_y of WJ-8C fastener is generally 2~3 mm, while the longitudinal ultimate resistance and the transverse resistance F_y of fastener is 15 kN and 75 kN, respectively [37]. And By referring the work of Wei et al. [38] and, the values of F_y and the d_y of the CA mortar layer and the lateral block are also summarized in Table 4.

As well, three spans of simply supported girders with lengths of 32 m, situated at the approach bridge, are set at both ends of the continuous bridge to take boundary constraints into fuller consideration.

In addition, the damping ratio of concrete beam bridge shall not be greater than 0.05 [22], thus a fixed Rayleigh

damping ratio of 5% is applied on the following time history analysis.

3.3 Earthquake input

The seismic safety assessment report at the bridge site shows that the shear wave velocity of the soil layer is greater than 500 m/s. According to the Chinese criterion [21, 22], the soil at the bridge site is defined as stiff soil since the stiff soil corresponds to shear wave velocity being greater than 500 m/s, and the characteristic period T_g is defined as 0.25 s with a seismic fortification intensity of grade eight. Based on this, 20 seismic waves with the best matching average response spectrum and design response spectrum are selected from the PEER seismic wave database as seismic

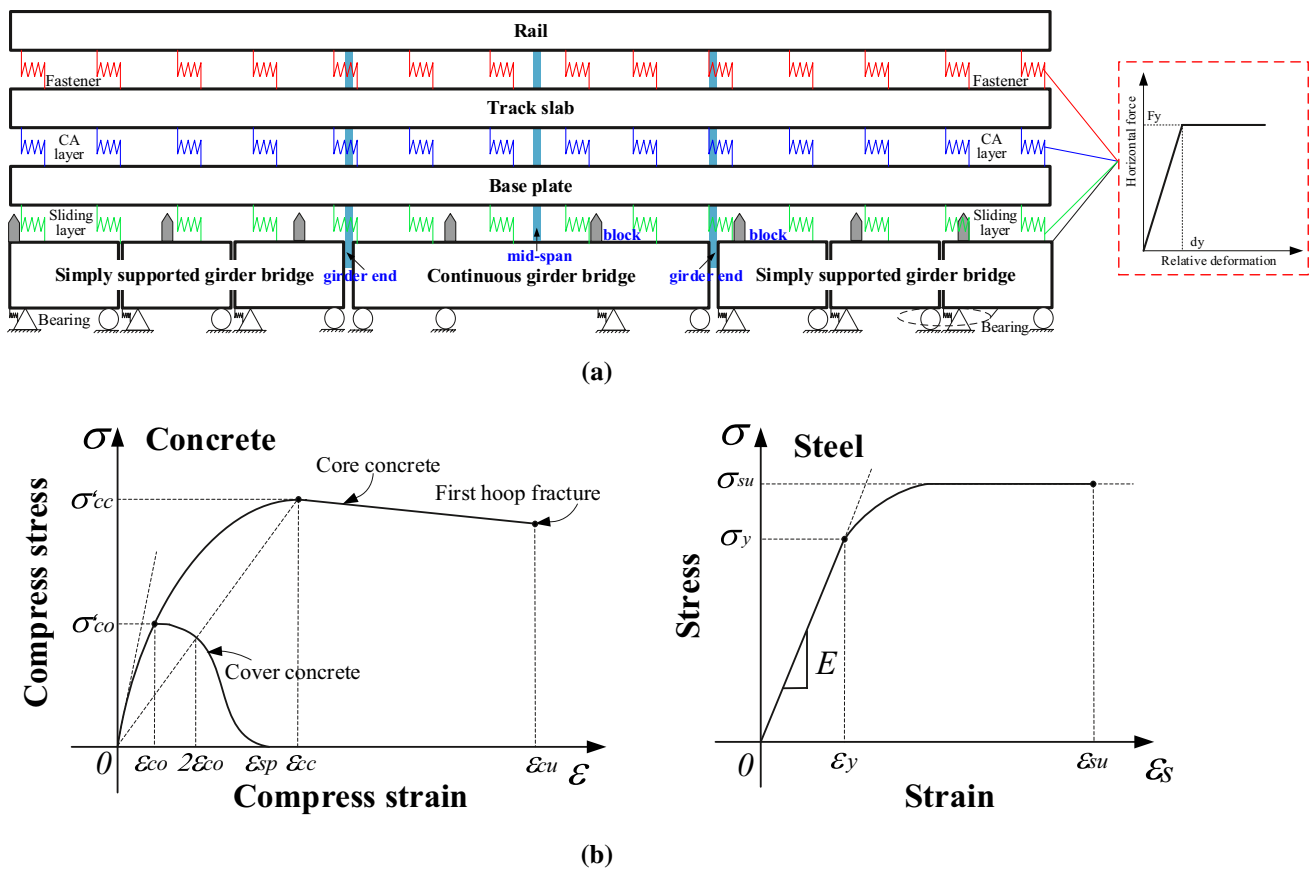


Fig. 4 Bridge model: (a) overall model and the load–displacement relations of the connect components for the idealized zero springs and (b) the load–displacement relations of concrete and steel material

Table 2 Key parameters of concrete materials [35]

Concrete components	Peak compressive stress f'_{cc} (MPa)	Peak strain ϵ_{cc}	Ultimate compressive strain ϵ_{cu}
Piers	29.3250	0.0035	0.01818
Piles- ϕ 1.25 m	26.5898	0.0024	0.00566
Piles- ϕ 1.50 m	26.3905	0.0023	0.00536

Table 3 Key parameters of longitudinal steel materials [36]

Steel components	Elastic modulus E (GPa)	Yield stress σ_y (MPa)	Yield strain ϵ_y	Maximum stress σ_{su} (MPa)	Maximum strains ϵ_{su}
Piers	200	385.5	0.00192	571	0.09
Piles	200	385.5	0.00192	571	0.09

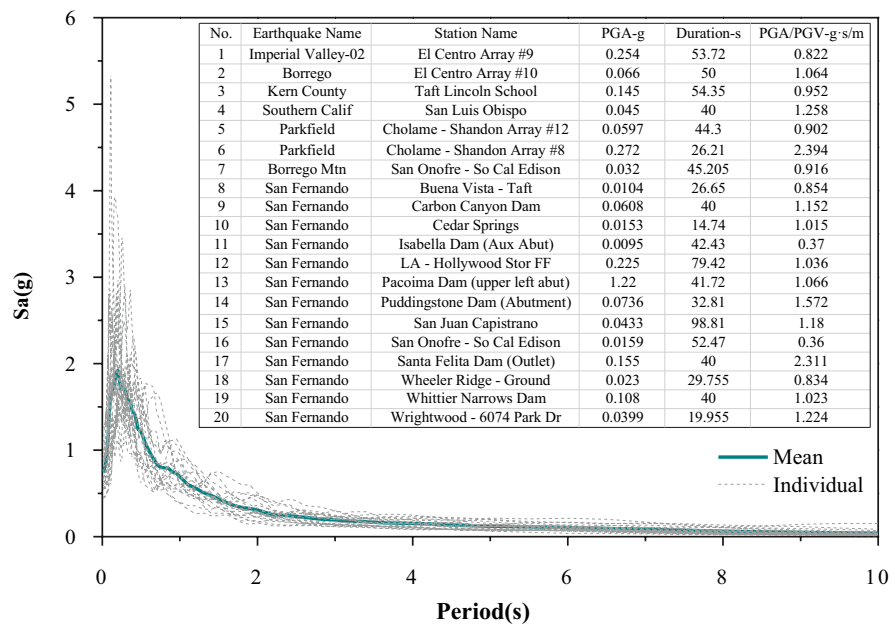
Table 4 Key parameters of connect components for the finite element model

Link components	Horizontal force F_y (kN)	Relative deformation D_y (m)
Fixed bearing [22]	5000	0.002
Sliding bearing [22]	470	0.002
Sliding layer [33]	6	0.0005
CA mortar layer [33]	41.52	0.0005
Fastener [37]	15 (in longitudinal)	0.002
Fastener [37]	75 (in transverse)	0.002
Block [38]	453.36	0.002

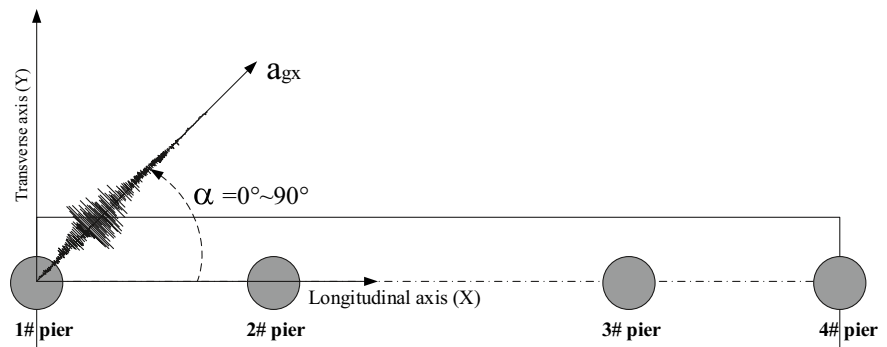
inputs, as depicted in Fig. 5a. Naeim [39], Idriss [40] and Mohraz [41] have carried out plenty of studies on the effects of soil conditions on ground motion characteristics and the

nature of spectral shapes. Seed and Idriss [42] discovered that the propagation of ground motion acceleration in hard soil is not significant, so the effects of soil density on the horizontal vibrations in the soil model are not studied in this paper. The seismic wave selected here is only considered from the matching degree between the average response spectrum and the design response spectrum without limiting the site conditions corresponding to the bridge site.

Fig. 5 Earthquake inputs: (a) ground motions and (b) incident angle of ground motion



(a)



(b)

Therefore, several selected records corresponding to the soil layer are not consistent with the soil condition at the bridge site, such as Imperial Valley, San Fernando and Parkfield. According to research results presented by Wei et al. [43, 44], spectral acceleration (S_a) as IM is suitable for high-speed railway bridges because it can greatly reduce the dispersion of its seismic response. In this paper, the structural seismic fragility curves are obtained using the IDA analysis method. Then, peak ground accelerations (PGA), which is equal to the response spectrum value of the structure vibrating with the ground, that is the response spectrum value corresponding to a certain period is equal to 0 s (S_{a0}) [45], are scaled, respectively, as 0.05 g, 0.1 g, 0.2 g, 0.4 g and 0.8 g. Correspondingly, the acceleration value of each acceleration record in the 20 ground motion records has also been adjusted using the same scale factor, generating 100 case analyses applying the IDA analysis method. Generally, earthquake inputs coincide with the axes of bridges in

longitudinal or transverse directions, however, in this study, the scaled 100 ground motions are fed into the case bridge at incident angles of 0° (along the longitudinal axis of the bridge), and 22.5° , 45° , 67.5° and 90° (along the transverse axis of the bridge) as shown in Fig. 5b.

Finally, 500 case analyses are carried out, with the results discussed in Sect. 4. All components responses of the whole bridge have been calculated but only representative EDPs are discussed due to limited space.

3.4 Damage index definition of components

The damage states (DS) of the structure can be defined as: an intact state (DS1), slight damage state (DS2), moderate damage state (DS3), severe damage state (DS4), and complete damage state (DS5). For the above engineering demand parameters, the damage index defined in a previous study is used in this paper, as shown in Table 5.

Table 5 Damage indexes of different components

Material of component	Boundary indexes			
	Intact (DS1) to slight (DS2)	Slight (DS2) to moderate (DS3)	Moderate (DS3) to severe (DS4)	Severe (DS4) to complete (DS5)
Cover concrete strain of piers and piles[49]	0.0006	0.002	0.0035	0.006
Core concrete strain of piers and piles[49]	0.0035	0.004	ϵ_{cu}	$1.5\epsilon_{cu}$
Steel bars strain of piers and piles[49]	0.01	0.015	$0.5\epsilon_{su}$	0.09
Sliding bearing (mm) [50]	100	130	160	200
Fixed bearing (mm) [50]	2	4	6	8
Sliding layer (mm) [38]	0.5	1	1.5	2
CA mortar layer (mm) [38]	0.5	1	1.5	2
Fastener (mm) [38]	2	3	4	5

Material strain and curvature can be used to define the damage state of concrete components [46, 47]. Zhong et al. [48] indicated that the section curvature is affected by axial compression. In light of this, material strain is considered for defining the damage index of similar piers as well as the piers in this study, with the threshold values between different damage states having been duly calculated [49] as listed in Table 3.

The definition of the damage index for the fixed bearings and sliding bearings can be referenced in Wei et al. [50]. Finally, the damage index of key components in the track structure, such as sliding layers, CA mortar layers and fasteners, are also found in the work of Wei et al. [38] given a lack of experimental data or seismic damage data on these components, findings which are also summarized in Table 5.

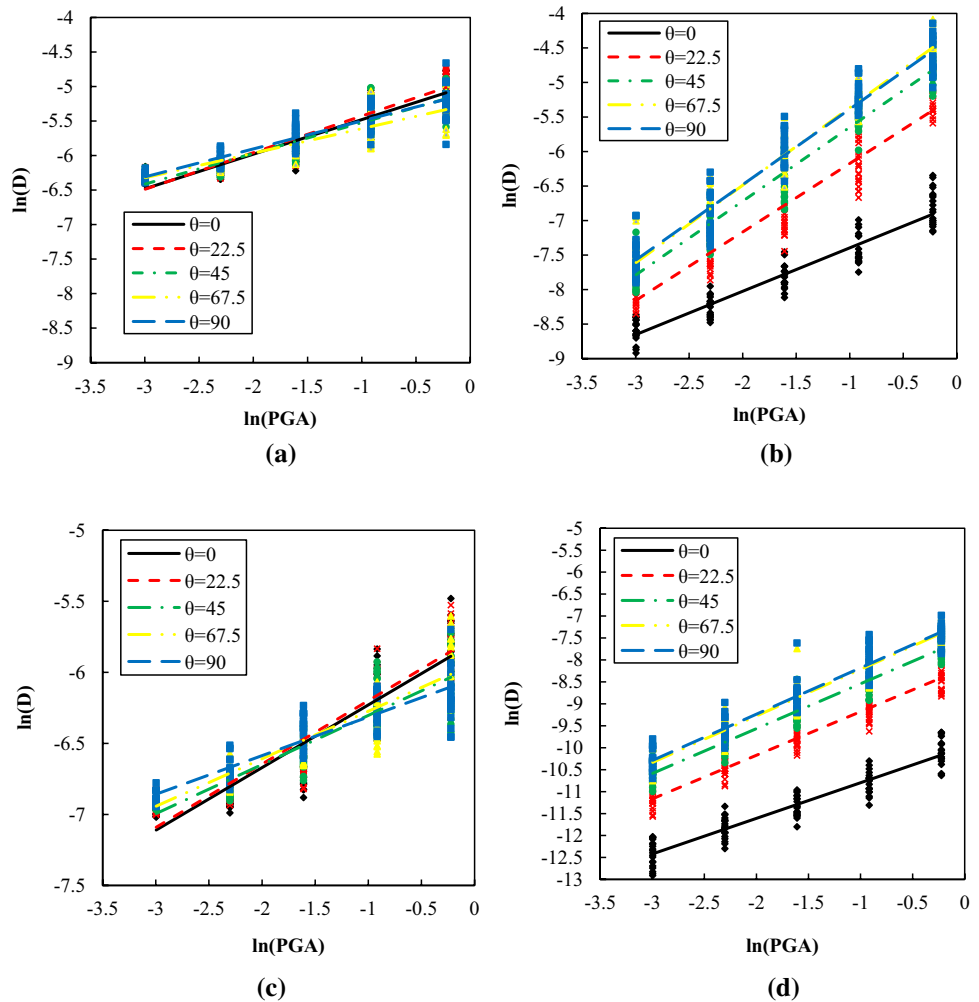
4 Calculation results

4.1 Seismic responses

Assuming seismic responses and PGA follow lognormal distributions, the linear regression analysis on the scatter plot of logarithmic seismic responses and PGA are conducted based on Eq. (2), i.e., probabilistic seismic demand model (PSDM). Therefore, the linear regression diagram of relative displacements for the sliding layer with different PGAs ranging from 0.05 g to 0.8 g and based on incident angles θ as in 0° , 22.5° , 45° , 67.5° and 90° are listed. Previous studies showed that the peak values of sliding layer appeared at the girder end and relative small values existed at mid-span [43]. Accordingly, the calculation results only at the two typical positions are depicts here, marked in Fig. 4a. In view of longitudinal response, Fig. 6 presents that the curves of PSDM under different intake angles of ground motions are close to each other. For instance, when PGA is 0.4 g, the average longitudinal responses of the sliding layer at the girder end corresponding to incident angles $\theta=0^\circ$ and 90° are 4.76 mm

and 4.51 mm, respectively, and with a maximum relative deviation of 5.25% (Actually, all the values of displacement and PGA are shown in Fig. 6 as logarithmic values. Under $\text{PGA}=0.4\text{ g}$ ($\ln(\text{PGA})=-0.916$), by converting 20 natural logarithms into its values and then averaging them, finally the response average value under $\text{PGA}=0.4\text{ g}$ with incident angles $\theta=0^\circ$ can be obtained.). Furthermore, the average longitudinal responses of the sliding layer at mid-span corresponding to $\theta=0^\circ$ and 90° are 2.17 mm and 1.94 mm, respectively, with a maximum relative deviation of 10.59%. This implies that the longitudinal displacement of the sliding layer is insensitive to the horizontal ground motion incident direction, and regardless of positioning whether at the girder end or at mid-span. This is because the longitudinal ground motions mainly excite the longitudinal vibration of the bridge, which causes the inconsistency of the longitudinal reciprocating vibration of the base plate and the girder, resulting in a larger longitudinal displacement of the sliding layer at the girder end. And transverse ground motions mainly excite the lateral bending modes of the bridge, which cause the girder end to slide inward while the track structure is restrained since the girder at the joint is disconnected but the track structure is continuous. Therefore, the girder and the base plate at the girder end have a relatively large longitudinal relative displacement. However, Fig. 6b, d show a pronounced increase in responses for the transverse direction with an increase in incident angles ($\theta=0^\circ-90^\circ$). Taking $\text{PGA}=0.4\text{ g}$ in Fig. 6b as an example, the average transverse displacement of the sliding layer at the girder end under $\theta=67.5^\circ$, 45° , 22.5° and 0° , decreased by 3.82%, 23.58%, 62.21% and 89.09%, respectively, as compared with the case of $\theta=90^\circ$. It should be noted that earthquakes with incident angles of 22.5° , 45° , 67.5° and 90° generate both longitudinal displacement and transverse displacement. That is to say, the coupling phenomenon is a significant seismic response for the sliding layer in longitudinal and transverse directions under earthquake scenarios with incident angles of 22.5° , 45° , 67.5° and 90° , and especially at the girder

Fig. 6 PSDMs for sliding layer: (a) longitudinal responses at girder end; (b) transverse responses at girder end; (c) longitudinal responses at mid-span; and, (d) transverse responses at mid-span

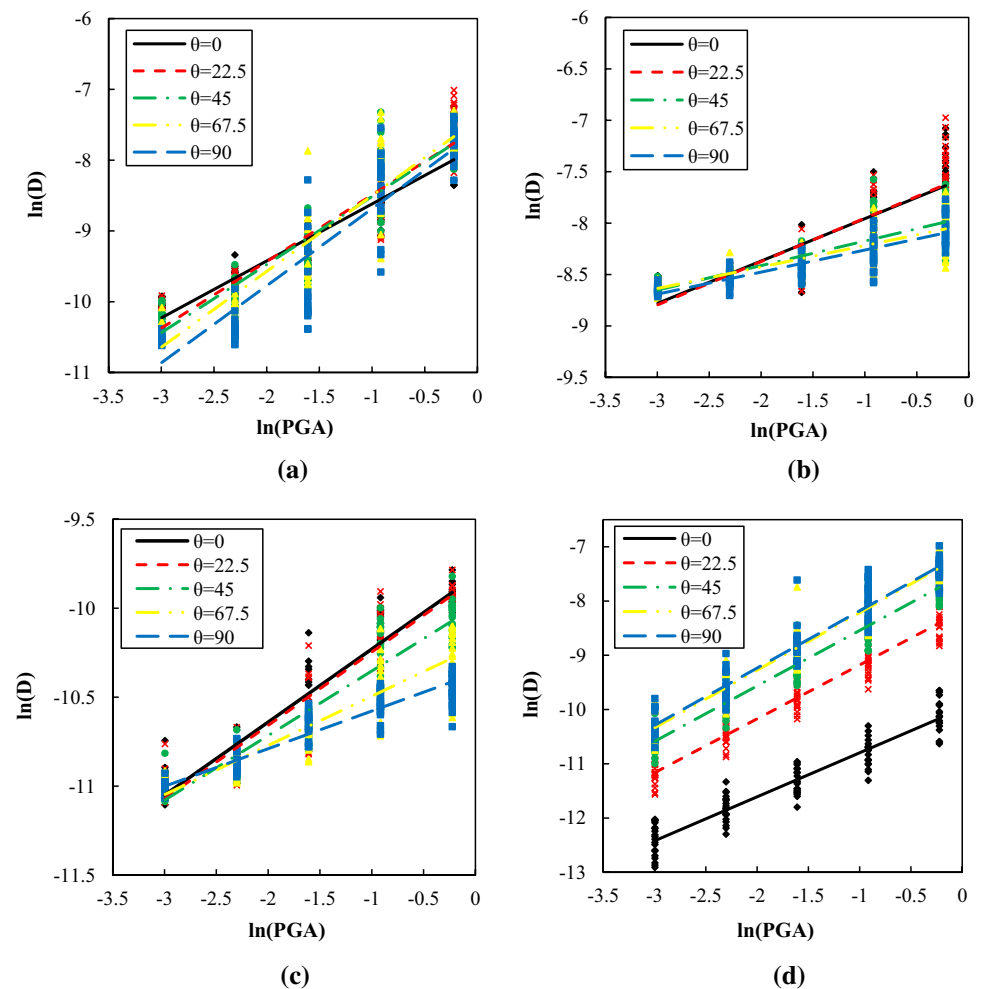


end. The reason for this is that the transverse component of ground motion generates transverse bending vibration on the continuous girder, while the track structure has to move along a longitudinal direction due to the restraints of lateral blocks, marked in Fig. 4a. Therefore, a coupling phenomenon happens under the transverse earthquake excitations. Another phenomenon is that the displacement of the sliding layer in a transverse direction almost reaches the maximum value when the incidence angle θ is 67.5° and 90° . For example, the estimated transverse displacement of $\theta=67.5^\circ$ varies within $\pm 5.2\%$ from that estimated for $\theta=0^\circ$ under $PGA=0.8$ g. This implies that when the ground motion is formed at a certain angle, the displacement response of the sliding layer caused by the coupling effect of the longitudinal and transverse directions of the bridge may be greater than that caused by inputs derived along transverse directions alone.

Figure 7 presents the probabilistic seismic demand model of the CA mortar layer with different incident angles. The average displacement of the CA mortar layer at the girder end is less than 0.1 mm as the PGA is less than 0.2 g. Thus,

it is appropriate to consider that the variation of incident angles on ground motion can be neglected. When PGA is less than 0.2 g, the displacement demand response of the CA mortar layer near the pier No. 3 indicated no changes based on different incident angles, while the displacement demand decreased with incident angles within the range of 0.2 ~ 0.8 g, as shown in Fig. 7b. The reason is that the shear tooth groove used to connect the girder and the base plate is set on the upper part of the girder position of pier No. 3. When the PGA is less than 0.1 g, the shear studs in the shear tooth groove are in an elastic state, and the CA mortar layer only slightly deformed; when the PGA is greater than 0.2 g, the shear studs yield, causing the CA mortar layer begins to slide, so the influence of the attack angle of ground motions becomes obvious. The variation of displacement of CA mortar layer at mid-span with seismic attack angle is the same as that at the pier No. 3 position, as shown in Fig. 7c. And the displacement of the CA mortar layer at the mid-span position is smaller than that at the pier No. 3 position. This is because the sliding layer at the middle-span position acts as a fuse and enters ductile failure first to avoid damage to

Fig. 7 PSDMs for CA mortar layer: (a) longitudinal responses at girder end; (b) longitudinal responses near pier No. 3; (c) longitudinal responses at mid-span; and, (d) transverse responses at mid-span



the upper track structure. Also, there exists a pronounced increase in responses for the transverse direction with an increase in the incident angles ($\theta=0^\circ$ – 90°), as plotted in Fig. 7d. Taking $\text{PGA}=0.4$ g as an example, the average transverse displacement of the CA mortar layer at the mid-span under $\theta=0^\circ$ to 90° are 0.021, 0.117, 0.228, 0.320 and 0.362 mm, respectively.

The seismic responses of the No. 6 fixed bearing under earthquake waves produced with PGAs from 0.05 g to 0.8 g and incident angles from 0° to 90° is presented in Fig. 8. It shows that an increase in the incident angles of earthquakes leads to a significant increase in responses along the transverse direction, as demonstrated in Fig. 8b, and with a sharp decrease in responses along the longitudinal direction, as in Fig. 8 (a). By setting $\text{PGA}=0.8$ g for example, the average longitudinal displacement of the No. 6 fixed bearing under earthquake incident angles of 0° and 90° are 143.8 mm and 0.22 mm, respectively, while the average transverse displacement of the No. 6 fixed bearing under earthquake incident angles of 0° and 90° are 0.16 mm and 215.8 mm, respectively. This implies that earthquakes with incident angles

of 0° individually cause considerable longitudinal seismic responses on the No. 6 fixed bearing, similarly, earthquakes with incident angle of 90° only cause considerable transverse seismic response. This is because longitudinal ground motions mainly excite the longitudinal vibration mode, i.e., the longitudinal drift of the girder, which will cause large longitudinal displacement of the bearings, and so does the transverse ground motions. In other words, there are almost no coupling effects for longitudinal and transverse responses under earthquakes at any incident angle. The influence of seismic incident angles on the displacement response of other bearings is almost the same as or similar to those of the No. 6 fixed bearing, including the No. 1 sliding bearing, as depicted in Fig. 8c, d.

A similar trend is observed in the cover concrete strain at the bottom section in pier No. 3, with the longitudinal response depicted in Fig. 9. By setting $\text{PGA}=0.8$ g for example, the average longitudinal cover concrete strains of the pier No. 3 under earthquake incident angles of 0° and 90° are 7.77×10^{-4} and 1.02×10^{-4} mm, respectively, while the average transverse cover concrete strains of the

Fig. 8 PSDMs for bearings: (a) longitudinal values of No.6 fixed bearing; (b) transverse values of No.6 fixed bearing; (c) longitudinal values of No.1 sliding bearing; and, (d) transverse values of No. 1 sliding bearing

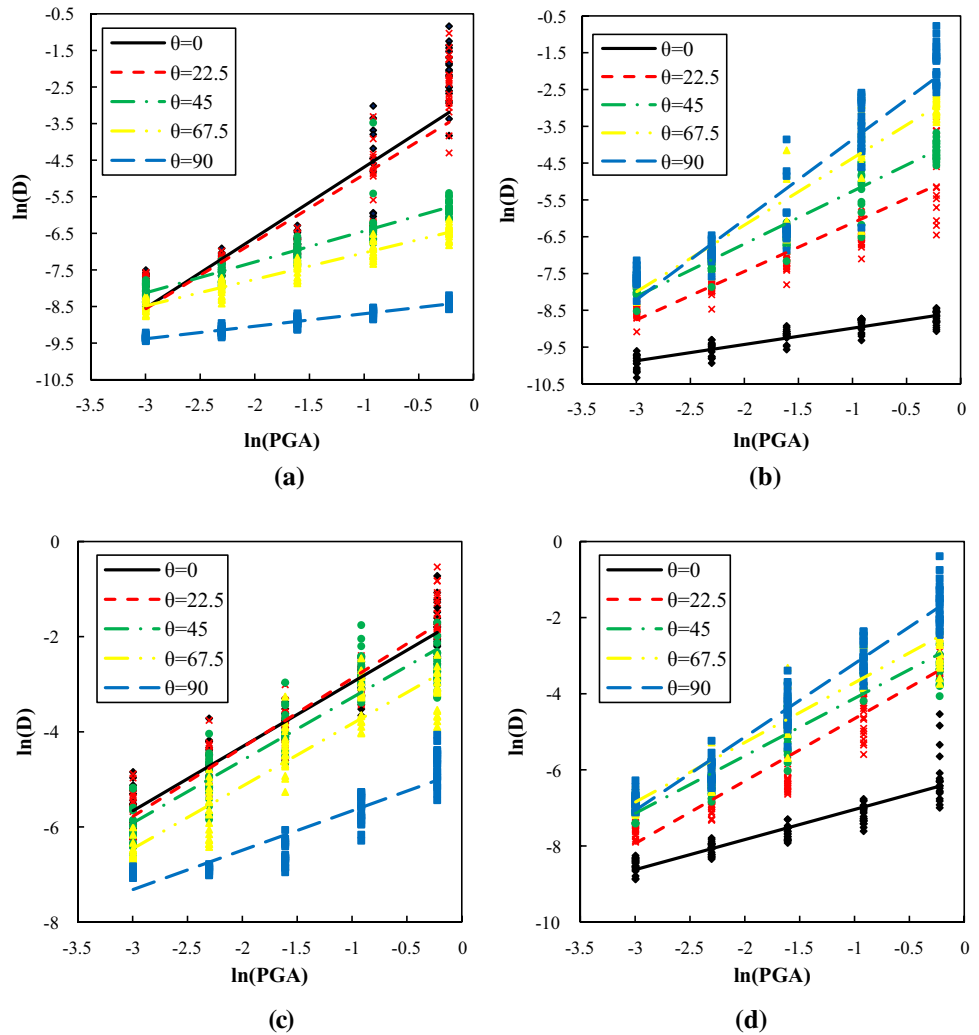
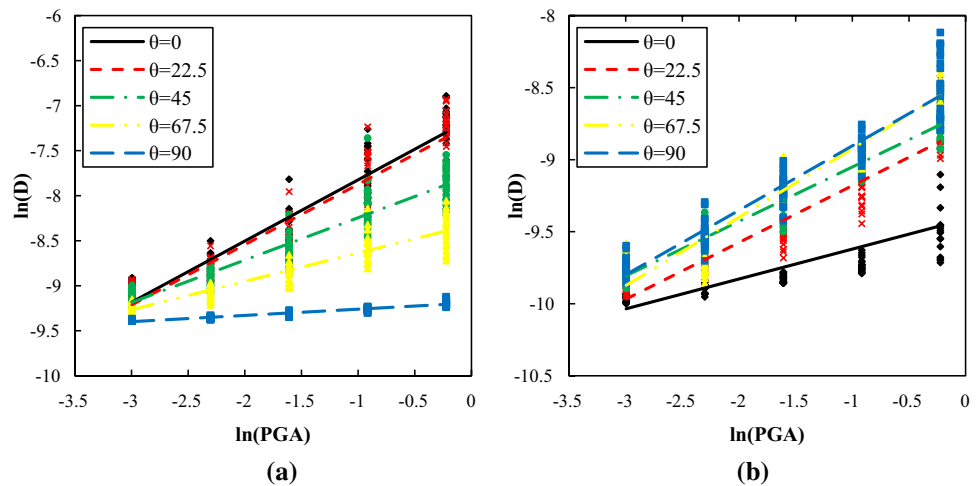


Fig. 9 PSDMs for pier No. 3: (a) longitudinal values and (b) transverse values



pier No. 3 under earthquake incident angles of 0° and 90° are 9.71×10^{-5} and 2.13×10^{-4} , respectively. This is because the piers mainly bear the shear force transmitted from the bearings, so the response of the piers changes with the input

angle of the ground motion in the same way as the bearings. Another reason is longitudinal ground motion mainly excites the longitudinal bending of the piers and the transverse ground motion mainly excites the lateral bending of

the piers. The cover concrete strains of other piers change according to the same rule as applied to those in Fig. 9. Since the responses of the confined concrete and steel bars of the piers were negligible, none of these values are listed herein.

4.2 Seismic fragilities

Utilizing linear interpolation, Fig. 10 shows the vulnerability surfaces of the sliding layer and the CA mortar layer at the girder end, being two representative components with coupling responses under earthquake scenarios. The orthogonal components of PGAs for any horizontal earthquakes are shown in x and y axes, and the x-axis represents the incident angles $\theta=0^\circ$, and the y-axis represents the incident angles $\theta=90^\circ$. The exceedance probabilities at any damage state are symmetric as in Fig. 10a, c. By

setting $PGA=0.8\text{ g}$ in Fig. 10a, as an example, the probabilities of the longitudinal sliding layer exceeding an extensive damage state (red surface) under incident angles $\theta=0^\circ, 22.5^\circ, 45^\circ, 67.5^\circ$ and 90° are found to be 98.7%, 99.2%, 98.1%, 96.1% and 98.0%, respectively. Compared with a case under incident angle $\theta=0^\circ$, the maximum deviation of probability exceeding extensive damage state is 2.63%, and the corresponding incident angle θ is 67.5° . This shows that a relatively smaller difference exists in the exceeding probability of the longitudinal displacement of the sliding layer and that of the CA mortar layer when acted upon by ground motions at any incident angles. However, exceeding probabilities of the transverse responses of the two components increased under seismic cases with θ ranging from 0° to 90° , as plotted in Fig. 10b, d. This is because it has been shown in PSDM that the transverse displacement of sliding layer increases with incident angle, so the

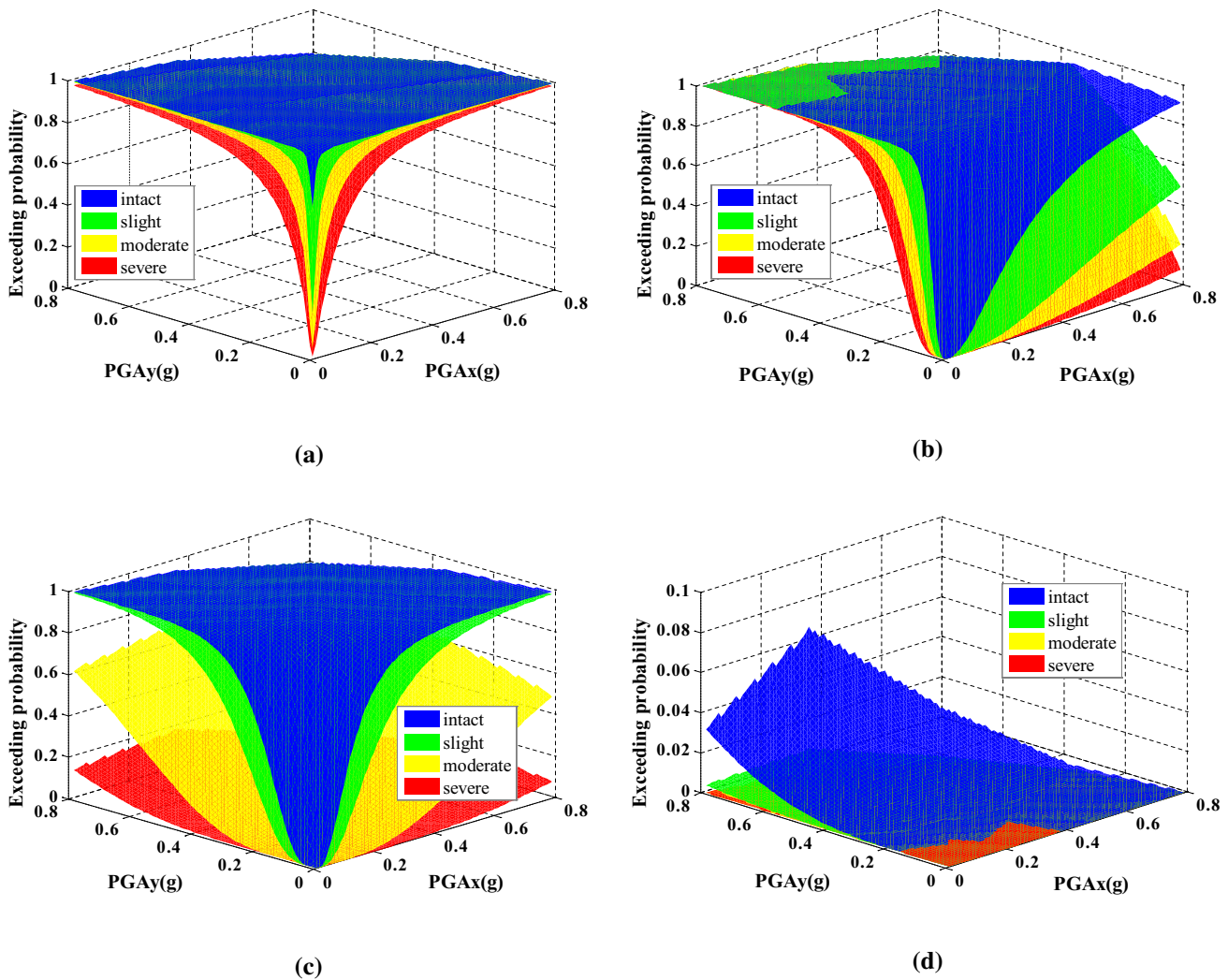


Fig. 10 Vulnerability surfaces of the sliding layer and CA mortar layer at the girder end: (a) longitudinal values of sliding layer; (b) transverse values of sliding layer; (c) longitudinal values of CA mortar layer; and, (d) transverse values of CA mortar layer

damage exceeding probability obtained by PSDM also shows the same law. Setting $PGA = 0.8$ g as in Fig. 10b in another example, the probabilities of the transverse sliding layer exceeding an extensive damage state (red surface) under incident angles $\theta = 90^\circ, 67.5^\circ, 45^\circ, 22.5^\circ$ and 0° are found to be 99.97%, 99.96%, 99.76%, 94.74% and 8.29%, respectively. And when compared to a case under incident angle $\theta = 90^\circ$, the probability of the transverse sliding layer exceeding an extensive damage state under $\theta = 67.5^\circ, 45^\circ, 22.5^\circ$ and 0° decreases by 0.01%, 0.21%, 5.23% and 91.71%, respectively. The longitudinal vibration mode excited by the longitudinal component of the ground motion has little effect on the transverse displacement of the sliding layer, and the transverse component of the ground motion plays a key role in its displacement. However, both the longitudinal and transverse components of ground motion contribute to the longitudinal displacement of the sliding layer. Thus, it can be concluded that the damage sensitivity arising from the transverse response of sliding layers and CA mortar layers to seismic incidence angles is more amplified than that of the longitudinal response. Another phenomenon is that the transverse damage exceeding probability of sliding layer is higher than that of CA mortar layer at girder end. This is because the sliding layer at the girder end is destroyed first in case of an earthquake, which dissipates seismic energy and avoids the failure of CA mortar layer. Moreover, the CA mortar layer at the girder ends works together with the shear reinforcements between the base plate and track slab, so the damage exceeding probability is low.

Figure 11 shows the vulnerability surfaces of the No. 6 fixed bearing, being one such case representative of components with uncoupling responses under earthquake scenarios. The exceedance probabilities at any damage state are asymmetric as shown in both Fig. 11a, b. Based on this, it

is clear that when the ground motions of $PGA = 0.8$ g form along 0° , the probability of exceeding each damage state in the longitudinal axis of the fixed bearing reaches 100%, while along 90° , the probability of exceeding is almost 0, as shown in Fig. 11a. On the contrary, when ground motions with $PGA = 0.8$ g form along 0° , the probability of the fixed bearing exceeding each damage state in the transverse direction is almost 0, while along 90° , the probability of exceeding each state reaches 100%, as shown in Fig. 11b. These phenomena indicate that the bearing damage is very sensitive to the incident angles of ground motion. This is consistent with the law of the influence of seismic attack angle on the response of bearings shown in the PSDM in Sect. 4.1.

A similar trend is observed in pier No. 3 at all damage states, plotted in Fig. 12. When taking $PGA = 0.8$ g as in Fig. 12a, for example, the probabilities of the longitudinal cover concrete exceeding an intact damage state under incident angles θ at $0^\circ, 22.5^\circ, 45^\circ, 67.5^\circ$ and 90° are found to be 59.7%, 55.2%, 17.9%, 2.6% and 0.02%, respectively. This indicates that the vulnerability of the pier is sensitive to the incident angles of ground motion. Hence, it is obvious that the damage to the pier in the transverse direction is amplified to a much lower degree. This is because the pier No. 3 resists the seismic force together with other piers under a transverse earthquake scenario, while pier No. 3 individually resists most of the seismic force in the longitudinal direction since the longitudinally fixed bearings (No. 5 and No. 6 fixed bearing) are only installed on the pier No. 3 as shown in Fig. 2.

4.3 Seismic risk assessment

Based on Eq. (8), the seismic risk probabilities for the different damage states of typical components at a basic seismic intensity of 8 degrees are shown in Figs. 13, 14,

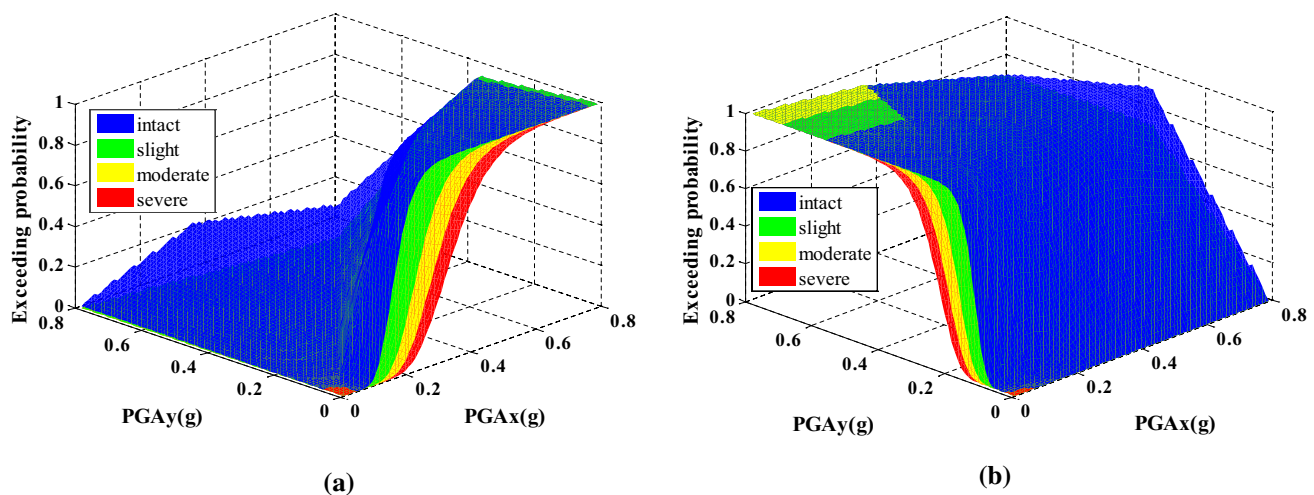


Fig. 11 Vulnerability surfaces of the No. 6 fixed bearing: (a) longitudinal direction and (b) transverse direction

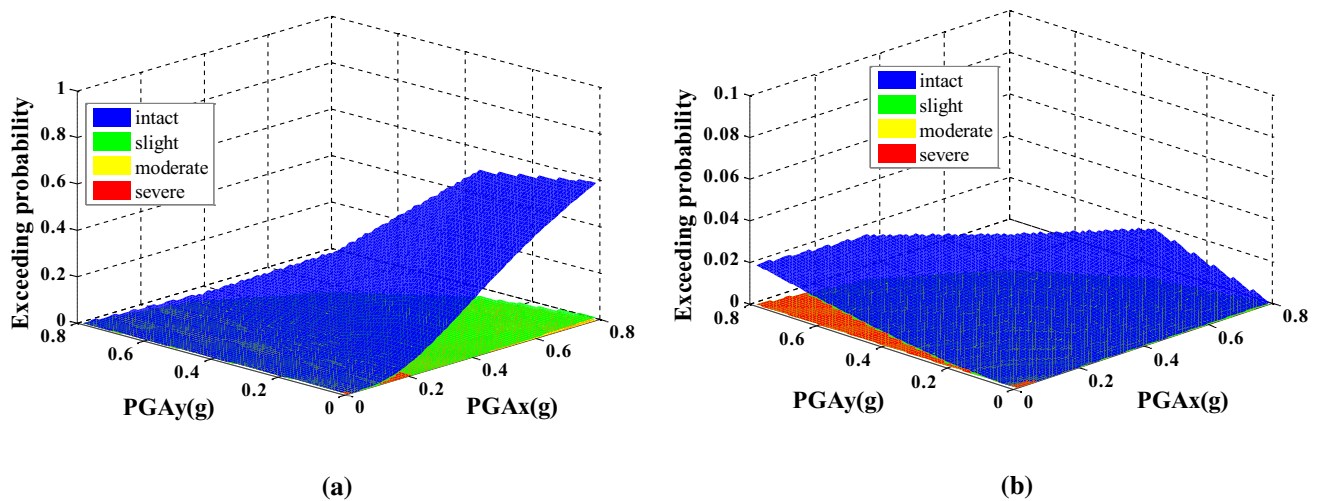
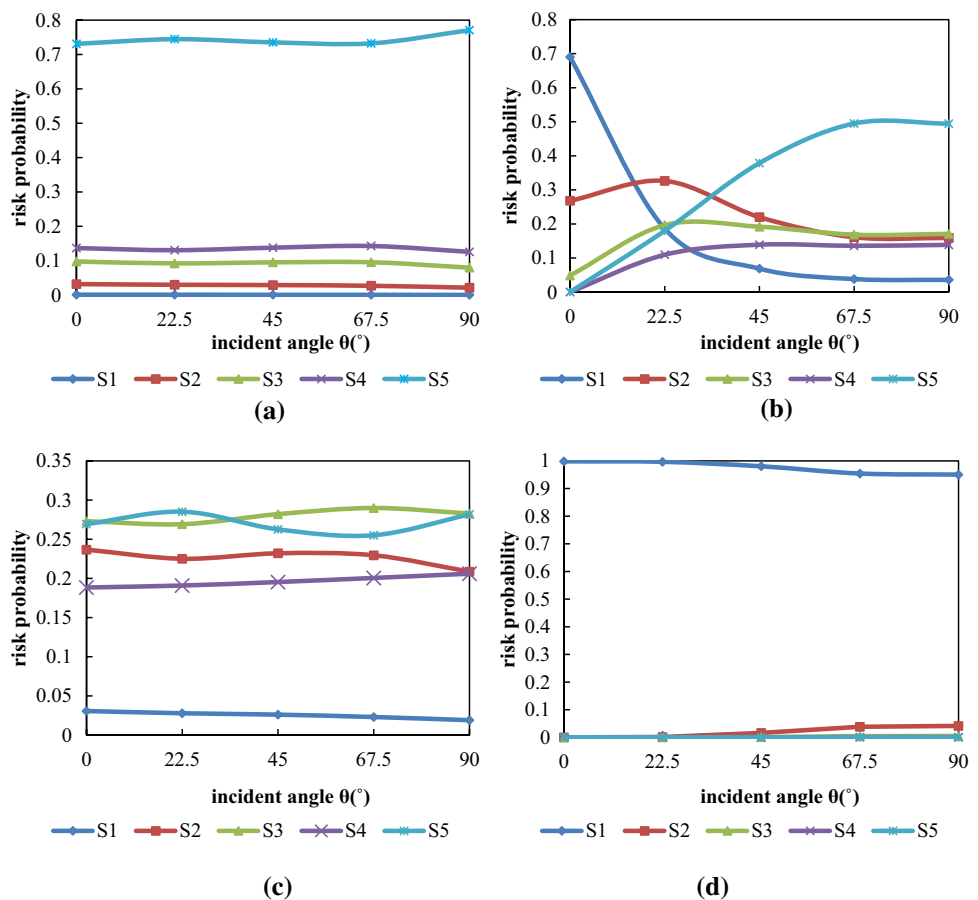


Fig. 12 Vulnerability surfaces of the pier No. 3: (a) longitudinal direction and (b) transverse direction

Fig. 13 Seismic risk probabilities at the different damage states of the sliding layer: (a) longitudinal values at girder end; (b) transverse values at girder end; (c) longitudinal values at mid-span; and, (d) transverse values at mid-span



15, 16, with these values taking into consideration the occurrence probability of each earthquake intensity level as shown in Table 1 at the bridge site. S1, S2, S3, S4 and S5, respectively, represent the five damage state.

Figure 13a, c indicates that earthquakes with an incident angle of 90° lead to seismic risk probabilities at different damage states of the sliding layer closer to those with other incident angles. Taking the risk probability of complete

Fig. 14 Seismic risk probabilities at the different damage states of the CA mortar layer: (a) longitudinal values at girder end and (b) longitudinal values near pier No. 3

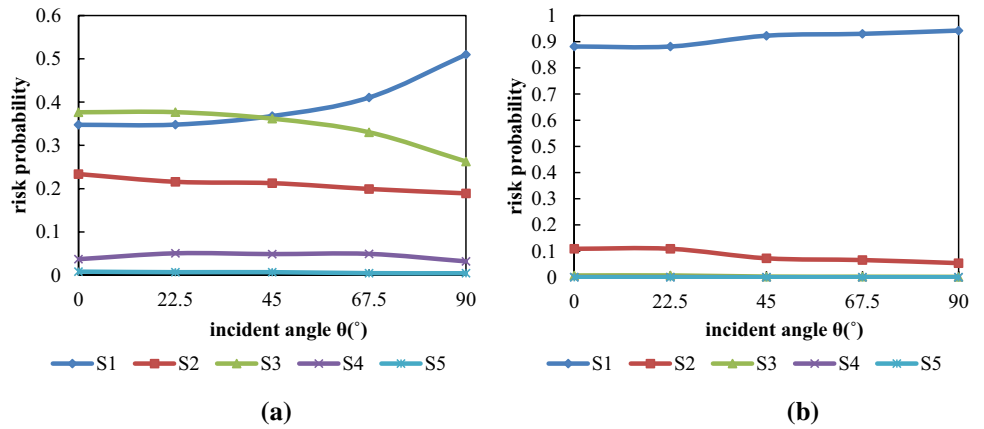


Fig. 15 Seismic risk probabilities at the different damage states for No. 6 fixed bearings: (a) longitudinal values and (b) transverse values

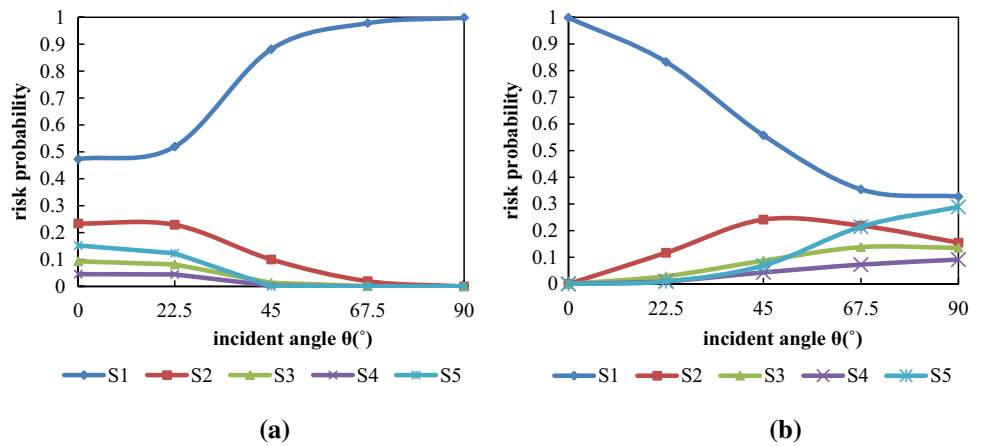
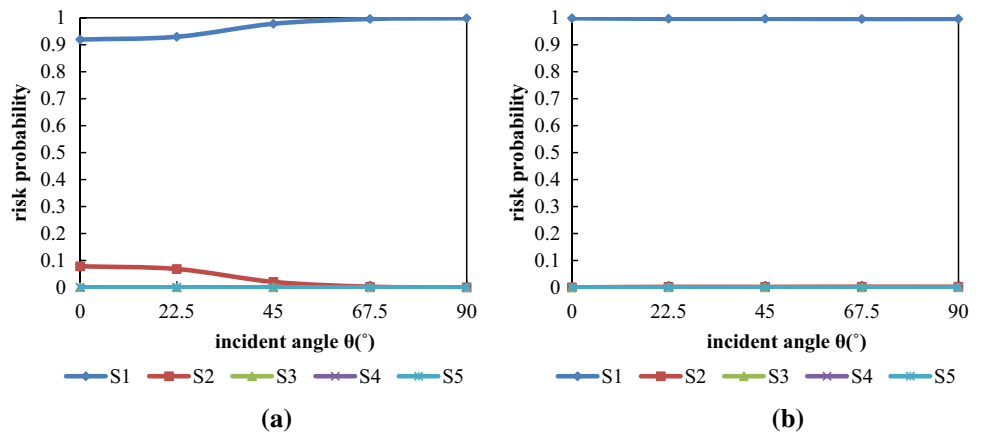


Fig. 16 Seismic risk probabilities at the different damage states for pier No. 3: (a) longitudinal values and (b) transverse values



damage to the sliding layer longitudinally as an example, the relative deviation of the risk probability caused by variability in incident angles θ is within 5.95%. This phenomenon also indicates that the seismic risk probability of different longitudinal damage states of the sliding layer is not sensitive to the seismic incident angle, regardless of whether it is at the girder end or at the mid-span position. The reason is that the exceeding probability of the longitudinal displacement of

the sliding layer is close to each other when acted upon by ground motions at any incident angles, and is seismic risk probabilities related to the damage exceeding probability, listed in Eq. (8). Therefore, a relatively smaller difference exists in the risk probability. However, as the incident angles of earthquakes increase, the probabilities at the complete damage state increase while the probabilities at the intact state decrease for the sliding layer at the girder end and the

mid-span in the transverse direction in Fig. 13b, d. In other damage states, the risk probability also varies significantly with the change of seismic input angle. It indicates that the risk probability of transverse damage to the sliding layer is more sensitive to the variability of θ . Another phenomenon is that the risk probabilities of transverse damage to the sliding layer reach a peak value and no longer change when the seismic incident angle is greater than 67.5° . For instance, compared with $\theta=67.5^\circ$ in Fig. 13b, the seismic risk probability of a moderate, severe and complete damage state for the sliding layer with $\theta=90^\circ$ increases by 1.79%, 1.47% and 0%. This implies that the maximum damage of the sliding layer is caused by ground motions formed with horizontal orientations between 67.5° and 90° along the bridge's longitudinal axis.

In addition, the seismic risk level at the girder end is always much higher than that at the mid-span regardless of the incident angles of the ground motion. The reason for this is that the base plate is continuous at the girder end, while the girder itself is disconnected, causing an inconsistent deformation between the base plate and continuous bridge ones. To be more specific, the risk probabilities for the complete failure of the sliding layer are always larger than 70% at the girder end as in Fig. 13a, while those probabilities are always less than 30% at the mid-span as in Fig. 13c following the longitudinal direction. Furthermore, the seismic risk level of the longitudinal sliding layer is always much higher than that in the transverse direction regardless of the incident angles of earthquake scenarios, which is due to the restraint generated from the lateral blocks. Compared with the probabilities of complete failure in the longitudinal direction for the sliding layer at the girder end, those probabilities in the transverse direction are always less than 55% as shown in Fig. 13b.

Figure 14 illustrates the seismic risk probabilities of different damage states for the CA mortar layer in the longitudinal direction at the girder end and near pier No. 3. As the incident angle of the ground motion increases, the risk probabilities of damage along the longitudinal axis in the CA mortar layer decrease. By taking the moderate damage of the CA mortar layer at the location of the girder end as example, and compared with a case under $\theta=0^\circ$, the seismic risk probability under $\theta=22.5^\circ$, $\theta=45^\circ$, $\theta=67.5^\circ$, $\theta=90^\circ$, decreases by 0%, 3.93%, 12.35% and 30.52%, respectively. Moreover, the seismic risk probability of moderate damage to the CA mortar layer at the location of the girder end with a ground incident angle of 90° reached 26.27%. This indicates that the coupling effect also exists in the CA mortar layer, but that it is more insignificant than that of the sliding layer. Previous probabilistic seismic demand analyses demonstrated that the displacement demand response of the CA mortar layer near pier No. 3 showed no changes with different incident angles when the PGA was less than 0.2 g, and

when corresponding to the basic intensity of 8 degrees (in Table 1). Accordingly, the seismic risk probability of longitudinal damage to the CA layer near pier No. 3 as affected by the incident angles of ground motion, is negligible, as shown in Fig. 14b. In addition, the seismic risk level for the CA mortar layer at the girder end, due to the inconsistent deformation between the continuous bridge and the simply supported bridges, is always much higher than that near pier No. 3, wherein more seismic energy is transformed from the fixed bearings to the pier as well as the shear teeth in the sliding layer. Furthermore, the unlisted seismic risk levels for the CA mortar layer in other positions (apart from positions at the girder end, at mid-span and near pier No. 3) are much lower than those listed in Fig. 14, since the sliding action of the sliding layer protects the CA mortar layer.

Figure 15 shows the seismic risk probabilities at the different damage states of the No. 6 fixed bearing. As the incident angles increase, the seismic risk probabilities of fixed bearing longitudinal damage decrease except in the intact state, as plotted in Fig. 15a. However, those probability values change towards the opposite trendline when in the transverse direction, as shown in Fig. 15b. By taking the complete damage state as an example, and when the incident angle θ increases from 0° to 90° , the risk probability of complete damage to the fixed bearing in the longitudinal direction is reduced from 15.2% to 0%, while the risk probability in the transverse direction is increased from 0 to 28.9%. The reason is that ground motions with an incident angle of 0° and 90° , respectively, only cause considerable damage to fixed bearings along the longitudinal and transverse direction, which has been discussed in Sect. 4.1 and Sect. 4.2. Therefore, as the incident angle increases, longitudinal seismic risk probabilities, i.e. probabilities of occurrence, of intact state of the bearings increase while seismic risk probabilities of other damage state decrease, and the opposite trendline appears in transverse values. Another notable phenomenon is that the seismic risk probabilities of a moderate, severe and complete damage state almost reach the maximum extent when the incident angle is greater than 67.5° .

The damage risk probability of pier No. 3 varies with the incident angles of ground motion in the same way as the fixed bearings, but its seismic risk probability is lower than that of the bearings. For example, the maximum seismic risk probability of slight damage to pier No. 3 is only 7.8% while the risk probability of other damage states is close to 0.

When combined with seismic vulnerability surfaces and seismic risk probabilities, ground motions forming at horizontal orientations between 67.5° and 90° along the bridge's longitudinal axis indicate that the transverse damage exceedance probabilities of the sliding layer and the CA mortar layer reach their maximum, and with the seismic risk probabilities varying within 1.79%. Meanwhile, the longitudinal damage was found to be insensitive to the seismic incidence

angle — that is, the component damage probability is coincident under any incidence angle. Furthermore, with a basic intensity of 8° , the risk probability of complete damage to fixed bearings in the transverse direction is 28.92%, while seismic risk probabilities in the transverse direction at other damage states almost reach their maximum when the incident angle is greater than 67.5° . To sum up, when the ground motions form with horizontal orientations between 67.5° and 90° along a bridge's longitudinal axis, the damage exceeding probability and the risk probability of complete damage in the example of high-speed railway bridge systems will approach their maximum degree.

5 Conclusion and research perspectives

A bridge site is inevitably surrounded by several faults, which leads to the ground motions of earthquakes acting upon high-speed railway bridges in different horizontal directions. In light of this, this paper evaluates the effects of ground motion incident angles on a typical and common track-bridge and identifies the most unfavorable incident angle of horizontal ground motions by performing incremental dynamic analyses (IDA), seismic vulnerability analyses and seismic risk assessments. The analytical approach was developed by adopting the perspective of PGA and the main conclusions can be drawn as follows:

(1) The ground motions along the longitudinal axis of the bridge ($\theta=0^\circ$) only caused seismic responses in the longitudinal direction. However, ground motions with orientations other than in the longitudinal direction of the bridge will produce considerable longitudinal and transverse responses, i.e., coupling responses, and this coupling phenomenon is most pronounced in the sliding layer and CA mortar layer. Thus, the longitudinal seismic damage to these two components from transverse waves should receive greater attention in terms of seismic design since the exceeding probabilities and seismic risk probabilities at various incident angles θ are as high as the calculated value for $\theta=0^\circ$, and with a variation within 5.95%.

(2) The maximum variation of the longitudinal response and probability of the sliding layer and CA mortar layer is within 10.59% under various incident angles. However, there is a significant difference in the transverse response and probabilities arising from different incident angles. This means that the transverse damage of the track structure is more sensitive to ground motion directionality effects than the longitudinal damage.

(3) Compared with the track structure, the response of bridge structure components, such as bearings and piers, varies more drastically under various incident angles.

(4) Probability of exceeding damage states and the risk probability of a complete damage state are at their

maximum when ground motions form with horizontal orientations between 67.5° and 90° along a bridge's longitudinal axis.

This paper presents the resulting data in terms of PGA, with consideration of the soil conditions in China. Therefore, these analytical results are directly applicable to stiff soil sites in China only. So, this research can be expanded in several aspects. First, it would be useful to study other soil types. Another important advancement of the presented investigations would be the research on the impact of horizontal ground motion on seismic hazard assessments of the studied structure by conducting response spectrum analyses.

Acknowledgements This research was jointly supported by the National Natural Science Foundations of China under grant No. 51778635 and 51778630, the Research Program on Key Technology for the Seismic Design of Railway Bridge in Nine Degree Seismic Intensity Zone under grant No. KYY2018059 and the Fundamental Research Funds of Central South University under grant No.2019zzts285. The above support was greatly acknowledged.

Funding This research was jointly supported by the National Natural Science Foundations of China under grant No. 51778635 and 51778630, and the Fundamental Research Funds of Central South University under grant No.2019zzts285. The above support was greatly acknowledged.

Compliance with ethical standards

Conflict of interest The authors declare that they have no known competing financial interests or personal relationships that could have appeared to influence the work reported in this paper.

Ethical approval This article does not contain any studies with human participants or animals performed by any of the authors.

Ethics statement Some of the same drawings in this paper are refer to these two articles published in "Bulletin of Earthquake Engineering" and "International Journal of Civil Engineering", where those data have already been published [38, 43].

References

1. Mackie KR, Cronin KJ, Nielson BG. Response sensitivity of highway bridges to randomly oriented multi-component earthquake excitation. *J Earthq Eng*. 2011;15(6):850–76.
2. Ramanathan KN. Next generation seismic fragility curves for California bridges incorporating the evolution in seismic design philosophy. *Georgia Instit Technol*. 2012;12:20–34.
3. Taskari O, Sextos A. Multi-angle, multi-damage fragility curves for seismic assessment of bridges. *Earthq Eng Struct Dyn*. 2015;44(13):2281–301.
4. Moschonas IF, Kappos AJ. Assessment of concrete bridges subjected to ground motion with an arbitrary angle of incidence: static and dynamic approach. *Bull Earthq Eng*. 2013;11(2):581–605.
5. Banerjee Basu S, Shinozuka M. Effect of ground motion directionality on fragility characteristics of a highway bridge. *Adv in Civil Eng*. 2011. <https://doi.org/10.1155/2011/536171>.

6. Magliulo G, Maddaloni G, Petrone C. Influence of earthquake direction on the seismic response of irregular plan RC frame buildings. *Earthq Eng Eng Vib*. 2014;13(2):243–56.
7. Ni Y, Chen J, Teng H, Jiang H. Influence of earthquake input angle on seismic response of curved girder bridge. *J traffic and Transport Eng*. 2015;2(4):233–41.
8. Soltanieh S, Memarpour MM, Kilanehei F. Performance assessment of bridge-soil-foundation system with irregular configuration considering ground motion directionality effects. *Soil Dyn Earthq Eng*. 2019;118:19–34. <https://doi.org/10.1016/j.soildyn.2018.11.006>.
9. Noori HR, Memarpour MM, Yakhchalian M, Soltanieh S. Effects of ground motion directionality on seismic behavior of skewed bridges considering SSI. *Soil Dyn Earthq Eng*. 2019;127:105820. <https://doi.org/10.1016/j.soildyn.2019.105820>.
10. Torbol M, Shinozuka M. Effect of the angle of seismic incidence on the fragility curves of bridges. *Earthq Eng Struct Dyn*. 2012;41(14):2111–24.
11. Araújo M, Marques M, Delgado R. Multi directional pushover analysis for seismic assessment of irregular-in-plan bridges. *Eng Struct*. 2014;79:375–89.
12. Bhatnagar UR, Banerjee S. Fragility of skewed bridges under orthogonal seismic ground motions. *Struct Infrastruct Eng*. 2015;11(9):1113–30.
13. Wang YD, Ibarra L, Pantelides C. Effect of incidence angle on the seismic performance of skewed bridges retrofitted with buckling-restrained braces. *Eng Struct*. 2020;211:110411.
14. Jeon JS, Choi E, Noh MH. Fragility characteristics of skewed concrete bridges accounting for ground motion directionality. *Struct Eng Mech*. 2017;63(5):647–57. <https://doi.org/10.12989/sem.2017.63.5.647>.
15. Jiang C, Wei B, Wang D, Jiang L, He X. Seismic vulnerability evaluation of a three-span continuous beam railway bridge. *Math Problems Eng*. 2017. <https://doi.org/10.1155/2017/3468076>.
16. Li Y, Conte JP. Effects of seismic isolation on the seismic response of a California high-speed rail prototype bridge with soil-structure and track-structure interactions. *Earthq Eng Struct Dyn*. 2016;45(15):2415–34.
17. Yan B, Liu S, Pu H, Dai G, Cai X. Elastic-plastic seismic response of CRTS II slab ballastless track system on high-speed railway bridges. *Sci China Tech Sci*. 2017;60(6):865–71. <https://doi.org/10.1007/s11431-016-0222-6>.
18. People's Republic of China National Railway Administration (CNRA-PRC). Code for Design of High Speed Railway (including its explanation) (TB 10621–2014). China: China Railway Press; 2014.
19. He X, Wu T, Zou Y, Chen YF, Guo H, Yu Z. Recent developments of high-speed railway bridges in China. *Struct Infrastruct Eng*. 2017;13(12):584–1595. <https://doi.org/10.1080/15732479.2017.1304429>.
20. Yan B, Dai GL, Hu N. Recent development of design and construction of short span high-speed railway bridges in China. *Eng Struct*. 2015;100:707–17.
21. People's Republic of China Ministry of Railway (CMR-PRC). Code for seismic design of railway engineering (GB 50111–2006). Beijing: China Planning Press; 2006.
22. People's Republic of China Ministry of Transport (CMT-PRC). Guidelines for seismic design of highway bridges (JTJ/TB02–01–2008). Beijing: China Communications Press; 2008.
23. Tekie PB, Ellingwood BR. Seismic fragility assessment of concrete gravity dams. *Earthq Eng Struct Dyn*. 2010;32(14):2221–40.
24. Cornell CA, Jalayer F, Hamburger RO, Foutch DA. Probabilistic basis for 2000 SAC federal emergency management agency steel moment frame guidelines. *J Struct Eng*. 2002;128(4):526–33.
25. Hwang H, Liu JB, Chiu YH. Seismic fragility analysis of highway bridges. Mid-America: Mid-America Earthq Center Technical Report; 2001.
26. Ramanathan K, DesRoches R, Padgett JE. Analytical fragility curves for multispan continuous steel girder bridges in moderate seismic zones. *Trans Res Record*. 2010;2202:173–82.
27. Nielson BG. Analytical fragility curves for highway bridges in moderate seismic zones. Atlanta, GA: Georgia Institute of Technology; 2005.
28. Gao XW, Bao AB. Probability model of earthquake action and its statistical parameters. *Earthq Eng EngDyn*. 1985;01:15–24.
29. Shibata A. Prediction of the probability of earthquake damage to reinforced concrete building groups in a city. In: Proceedings of the 7th World Conference on Earthquake Engineering; 1980. p. 395–402.
30. State Seismological Bureau. Earthquake intensity zoning map of China. Beijing: Seismological Press; 1990.
31. Deierlein GG, Krawinkler H, Cornell CA. A framework for performance-based earthquake engineering. In: 7th Pacific Conference on Earthquake Engineering, vol. 273; 2003. p. 1–8.
32. Ministry of Transport of the People's Republic of China (MOT-PRC). Specifications for design of highway reinforced concrete and prestressed concrete bridges and culverts (JTJ 3362–2018). Beijing: China Communications Press; 2018.
33. TB10015-2012. Code for design of railway continuously welded rail. Beijing: China Railway Press; 2013.
34. Manual O. Open system for earthquake engineering simulation user command-language manual. Berkeley: Pacific Earthquake Engineering Research Centre University of California; 2009.
35. Mander JAB, Priestley MJN. Theoretical stress-strain model for confined concrete. *J Struct Eng*. 1988;114(8):1804–26.
36. Filippou FC, Popov EP, Bertero VV. Effects of Bond Deterioration on Hysteretic Behavior of Reinforced Concrete Joints. Report EERC 83–19. Berkeley: Earthquake Engineering Research Center University of California; 1983.
37. Dai GL, Liu WS. Applicability of small resistance fastener on long-span continuous bridges of high-speed railway. *J Central South Univ*. 2013;20(5):1426–33.
38. Wei B, Yang TH, Jiang LZ, He XH. Effects of uncertain characteristic periods of ground motions on seismic vulnerabilities of a continuous track-bridge system of high-speed railway. *Bull Earthq Eng*. 2018;16(9):3739–69. <https://doi.org/10.1007/s10518-018-0326-8>.
39. Naeim F. Seismic Design Handbook. 2001. <https://doi.org/10.1007/978-1-4615-1693-4>.
40. Idriss IM. Influence of Local Site Conditions on Earthquake Ground Motions Proc 4th US Nat Conf on Earthq Eng. California: Palm Springs; 1990.
41. Mohraz B. A study of earthquake response spectra for different geological conditions. *Bull Seism Soc Am*. 1976;66(3):915–35.
42. Seed HB, Idriss IM. Ground Motions and Soil Liquefaction During Earthquakes. Berkeley, California: Earthq Eng Research Inst; 1982.
43. Wei B, Li CB, He XH. The Applicability of Different Earthquake Intensity Measures to the Seismic Vulnerability of a High-Speed Railway Continuous Bridge. *Inter J Civil Eng*. 2019;17(7A):981–97. <https://doi.org/10.1007/s40999-018-0347-3>.
44. Biao W, Chengjun Z, Xuhui H, et al. Effects of vertical ground motions on seismic vulnerabilities of a continuous track-bridge system of high-speed railway. *Soil Dyn Earthq Eng*. 2018;115:281–90. <https://doi.org/10.1016/j.soildyn.2018.08.022>.
45. Vamvatsikos D, Cornell CA. Developing efficient scalar and vector intensity measures for IDA capacity estimation by incorporating elastic spectral shape information. *Earthq Eng Struct Dyn*. 2005;34(13):1573–600.

46. Hwang H, Jernigan JB, Lin YW. Evaluation of seismic damage to Memphis bridges and highway systems. *J Bridge Eng.* 2000;5(4):322–30.
47. Park YJ, Ang AHS. Mechanistic seismic damage model for reinforced concrete. *J Struct Eng.* 1985;111(4):722–39.
48. Zhong J, Pang YT, Jeon JS, Desroches R, Yuan WC. Seismic fragility assessment of long-span cable-stayed bridges in China. *Adv Struct Eng.* 2016;19(11):1797–812.
49. Kowalsky MJA. Displacement-based approach for the seismic design of continuous concrete bridges. *Earthq Eng Struct Dyn.* 2002;31(3):719–47.
50. Wei B, Hu ZL, He XH, Jiang LZ. Evaluation of optimal ground motion intensity measures and seismic fragility analysis of a multi-pylon cable-stayed bridge with super-high piers in mountainous areas. *Soil Dyn Earthq Eng.* 2020. <https://doi.org/10.1016/j.soildyn.2019.105945>.

Publisher's Note Springer Nature remains neutral with regard to jurisdictional claims in published maps and institutional affiliations.